nature nanotechnology

SUPPLEMENTARY INFORMATION

DOI: 10.1038/NNANO.2012.116

Deformation Mechanisms in nanotwinned metal nanopillars

Dongchan Jang,* Xiaoyan Li,* Huajian Gao, and Julia R. Greer

This file includes:

Supplementary Figures S1-S16;

Supplementary Discussions 1-3;

Supplementary Movies' Captions S1-S4;

References for Supplementary Information.

* These authors contributed equally to the work.

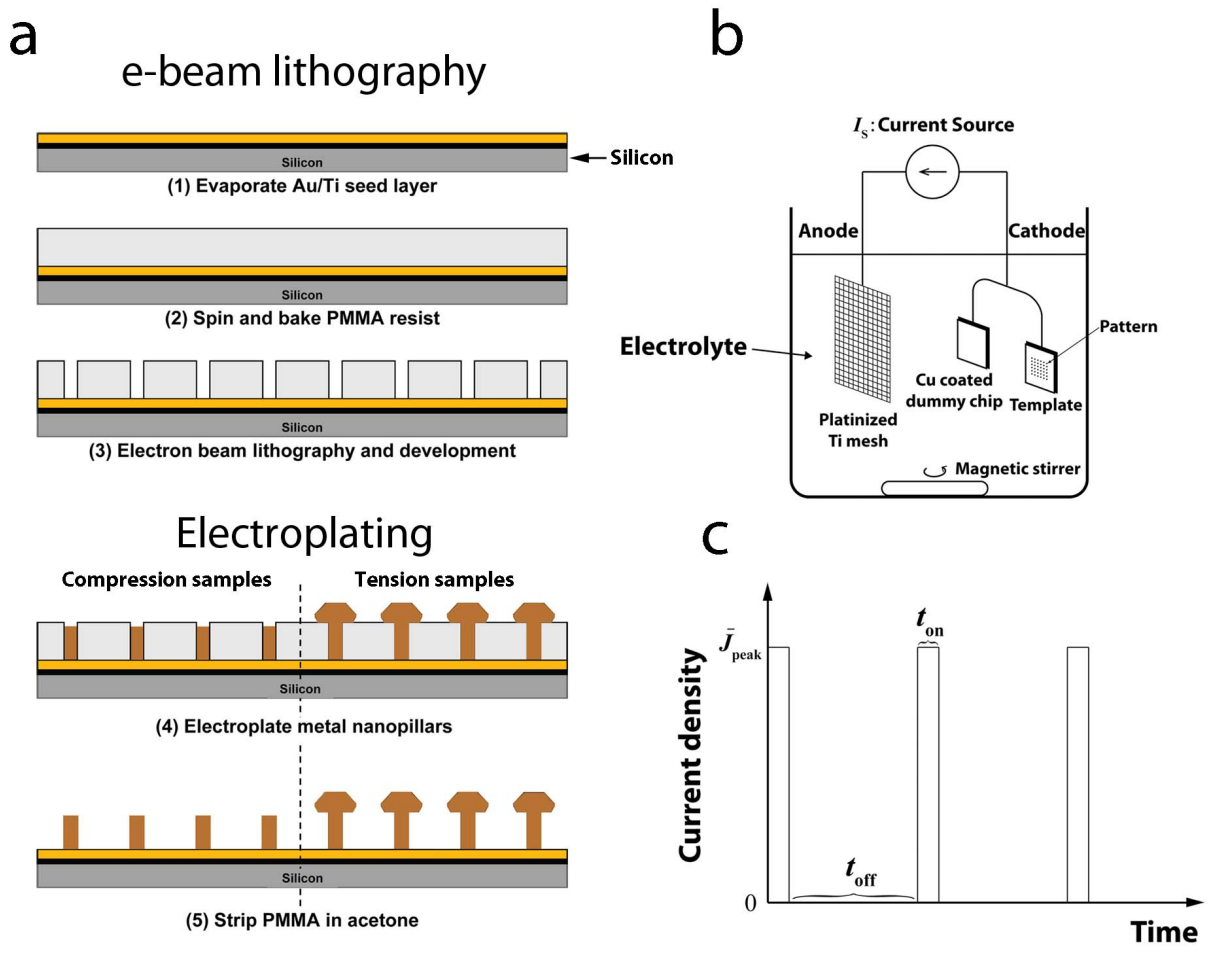

Supplementary Figure S1. **Fabrication procedure for nanotwinned nanopillars.** **a,** A schematic showing nanotwinned nanopillar fabrication steps (after Ref. [31] in Main Text). **b,** A schematic representation of the electroplating setup. **c,** The waveform of the pulsed electroplating current.

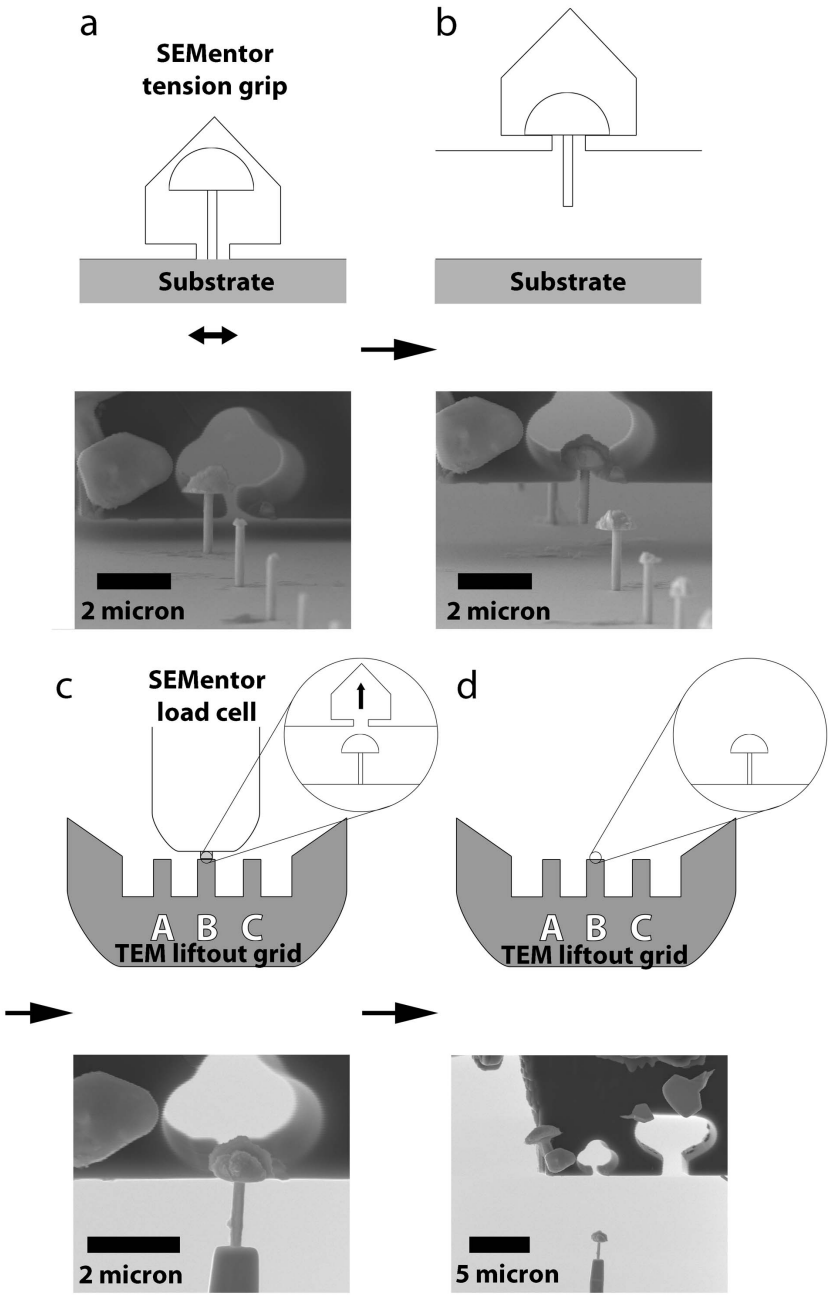

Supplementary Figure S2. **Plucking of individual samples for TEM analysis. a,** A nanopillar is placed within the SEMentor tension grip, and detached from the substrate by gently shaking the sample stage. **b,** The detached nanopillar is lifted up by the SEMentor tension grip. **c, d,** The lifted nanopillar is transferred on top of a post on the TEM lift-out grid.

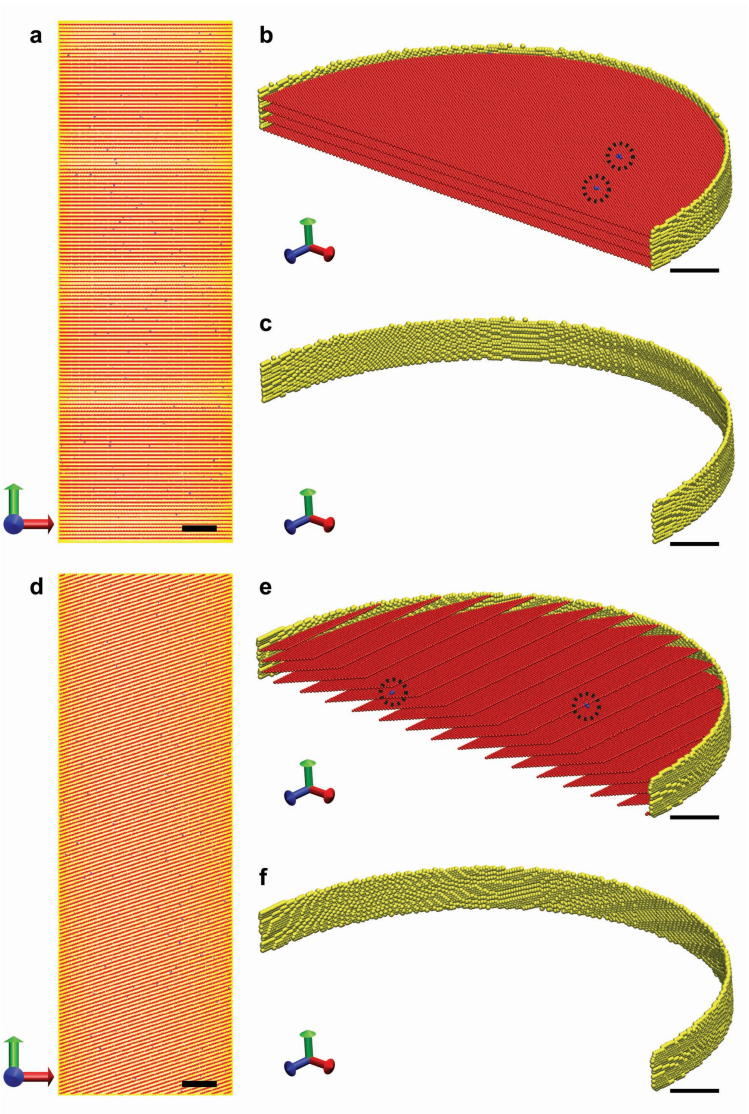

Supplementary Figure S3. **Representative initial atomic configurations of simulated nanopillars with the diameters of 50 nm and TB spacing of 1.05 nm after equilibration.** **a,** Front view of half nanopillar with orthogonal TBs. **b,** Perspective view of middle part of the sample in (**a**). **c,** Perspective view of free surface in the middle part of the sample in (**a**). **d,** Front view of half nanopillar with slanted TBs. **e,** Perspective view of middle part of the sample in (**d**). **f,** Perspective view of free surface in the middle part of the sample in (**d**). In (**b**) and (**e**), a number of vacancies are marked by circles. From (**c**) and (**f**), free surfaces in simulated samples are relatively polished but atomically rough. For clarity, fcc atoms are removed in all figures. Scale bars are 10 nm in (**a**) and (**d**) and 5 nm in all other figures.

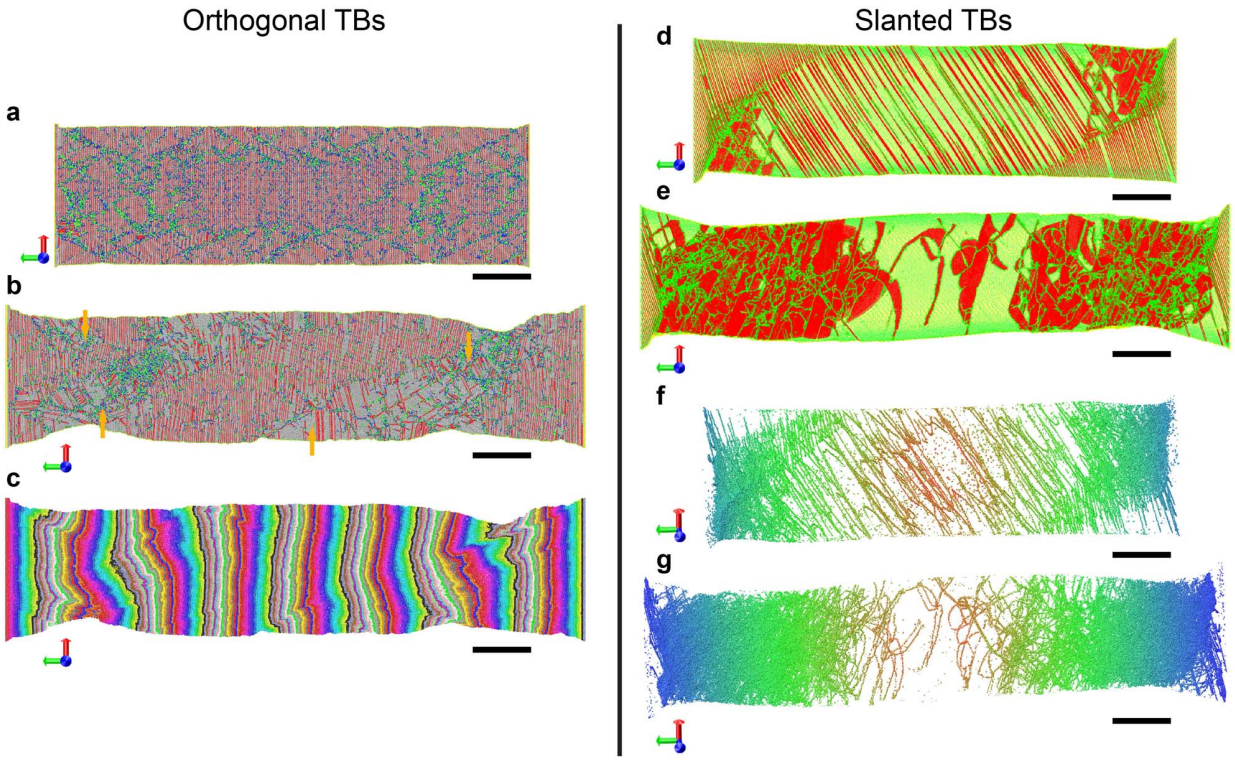

Supplementary Figure S4. **Atomic configurations of simulated nanopillars with the diameters of 50 nm and TB spacing of 0.63 nm during plastic deformation.** **a,** Atomic structures along the middle longitudinal section of the deformed sample at the strain of ϵ=10.52%. Most dislocations were nucleated from the intersections between the free surfaces and TBs. **b, c,** Atomic structures along the middle longitudinal section of the deformed sample at the strain of ϵ=34.98%. Shear bands are indicated by the orange arrows. **d, e,** Sectional views at the strains of ϵ=10.52% (**d**) and ϵ=34.98% (**e**). **f, g,** Dislocation structures at the strains of ϵ=10.52% and ϵ=34.98%, respectively. From (**d**)–(**g**), de-twinning is identified as the governing mechanism of nanotwinned nanopillars with slanted TBs. All scale bars are 20 nm. Atoms in (**a**), (**b**), (**d**) and (**e**) are rendered in the local crystal order method, while atoms in (**f**) and (**g**) are rendered in position-based coloring.

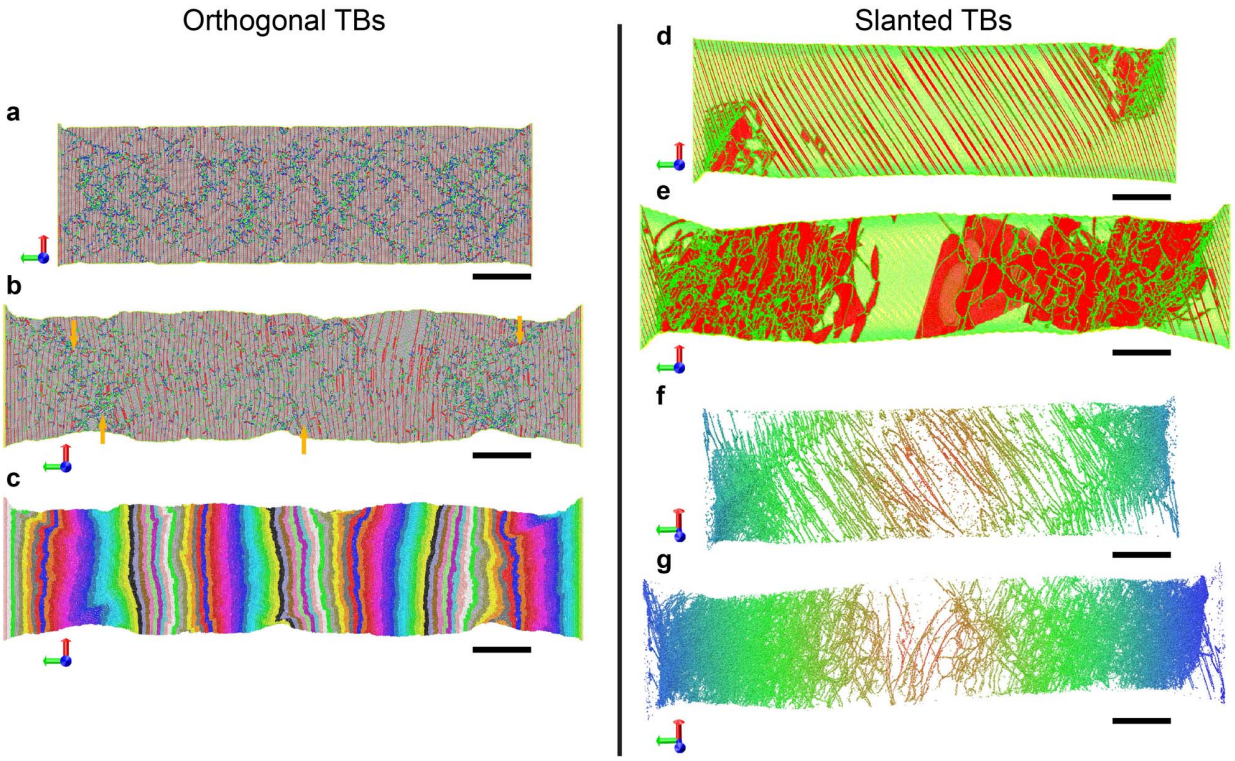

Supplementary Figure S5. **Atomic configurations of simulated nanopillars with the diameters of 50 nm and TB spacing of 1.25 nm during plastic deformation.** **a,** Atomic structures along the middle longitudinal section of the deformed sample at the strain of ϵ=10.52%. **b, c,** Atomic structures along the middle longitudinal section of the deformed sample at the strain of ϵ=34.98%. Shear bands are indicated by orange arrows. **d, e,** Sectional views at strains of ϵ=10.52% (**d**) and ϵ=34.98% (**e**). **f, g,** Dislocation structures at the strains of ϵ=10.52% and ϵ=34.98%, respectively. All scale bars are 20 nm. Atoms in (**a**), (**b**), (**d**) and (**e**) are rendered in the local crystal order method, while atoms in (**f**) and (**g**) are rendered in position-based coloring.

SUPPLEMENTARY DISCUSSION 1.

Influence of Oxide Layer on the Deformation of Nanotwinned Cu Nanopillars.

The native oxide layer formed on the outer surfaces of Cu nanopillars generally has the composition of Cu_2O and CuO (with Cu_2O usually occupying a larger fraction). In bulk ionic crystals, these oxides usually have lower moduli than the pure Cu[S1–S3]. In the present experiments, our TEM analysis indicated that the oxide layer on the Cu nanopillars was amorphous and likely formed when the samples were exposed to the ambient air. We have measured the thickness of the oxide layer to be about 5 nm.

Previous experimental studies[S4,S5] on the deformation of single-crystalline metallic nanopillars without the twins have demonstrated that the size effect on their strength was not caused by surface hardening due to the presence of the oxide layer. *In-situ* observations[S6] have revealed that the oxide layer was not able to trap the dislocations inside the nanopillars during deformation, in contrast to the intentionally deposited passivation[S7]. The size effect in the single-crystalline metallic nanopillars has been attributed to the progressive activation and exhaustion of dislocation sources and to dislocation starvation. This implies that, while its influence cannot be neglected, the native oxide layer likely does not significantly affect either the commencement of plasticity or the strength of the nanopillars. On the other hand, the oxide layer might influence the dislocation nucleation processes near the free surface. Our TEM analysis on the as-fabricated samples indicated that the samples were initially free of dislocations and nucleated mainly at the surface during the initial stage of plastic deformation. Therefore, the presence of the oxide layer might have caused some scatter in the peak stresses of tensile stress-strain curves, as would be expected for dislocation nucleation. Indeed, there exists a non-trivial amount of scatter in the strengths of the nanotwinned pillars. This amount of scatter is typical for the deformation of single-crystalline metallic nanopillars, which might have arisen from the variations in surface roughness and the presence of a native oxide layer.

SUPPLEMENTARY DISCUSSION 2.

Brittle and Ductile Fracture of Nanotwinned Cu Nanopillars.

We observe that the nanopillars with orthogonal twin boundaries undergo brittle fracture when the diameter D is 100 nm and the mean twin boundary spacing λ is 4.3 nm, while the nanopillars with D=50 nm/λ=1.2 nm, D=70 nm/λ=0.6 nm and D=250 nm/λ=2.8 nm fail by ductile necking with enhanced plasticity. Copper is typically a ductile metal that can undergo large plastic deformation. Therefore, it is surprising and intriguing that the nanotwinned Cu nanoplliars failed by brittle fracture. Several recent experimental studies also reported brittle fracture in single-crystalline metallic nanowires or nanowhiskers. For example, *in-situ* tensile tests on $[01\bar{1}]$ oriented Cu nanowhiskers (with D=75–282 nm) grown by physical vapor deposition[S8] have shown that some samples exhibited brittle fracture near their theoretical strength. Such brittle fracture at extremely high strength is thought to be due to the small sample size, the presence of atomically smooth, faceted surfaces and absence of initial dislocations[S8]. Recent experiments[S9] have also reported brittle fracture in the <111>-oriented Au nanowires (with D=5.5–14.0 nm), with fracture surface coincident with a twin plane oriented perpendicular to the tensile axis. *In-situ* HRTEM studies of post-mortem samples indicated that the brittle fracture originated from damage initiation and extension at the intersection between twin boundary and free surface[S9].

We note that in the present experiments, the nanotwinned pillars with D=100 nm and λ=4.3 nm failed without appreciable plastic deformation, and the fracture surfaces were nearly perpendicular to the tensile direction. In contrast, the nanotwinned pillars with D=50 nm and λ=1.2 nm showed extensive plastic deformation and strain localization for both orientations of twin boundaries – orthogonal and slanted – prior to fracture. To understand these different fracture modes, we have preformed a number of atomistic simulations to investigate fracture mechanisms in nanotwinned nanopillars.

A. Atomistic Simulations.

Recently reported theoretical and atomistic study[S10] showed an interesting directional anisotropy of the fracture mode along a coherent twin boundary $\Sigma3[1\bar{1}1]$ in Cu, i.e. brittle cleavage for a crack moving along $[1\bar{1}\bar{2}]$ in the twin plane but dislocation emission if it

attempts to move in the opposite direction. This suggests that coherent twin boundaries are intrinsically brittle and could serve as cleavage planes. Experiment[S9] showed that sub-20 nm Au nanowires fractured along a twin plane. Our present experiments also demonstrated that the brittle fracture occurred on the twin planes. We performed molecular dynamics simulations of crack propagation along a twin boundary in nanotwinned Cu to understand the distinct fracture modes observed in experiments.

In addition to the simulations described in the main text, we simulated a nanotwinned Cu slab with dimension of $50\times50\times2.55$ nm^3 (we have also conducted fully-3D MD simulations with much larger sample thickness in the out-of-plane direction to allow dislocation loops to be nucleated at the crack tip. These simulations show essentially the same behavior as the quasi-3D simulations). We studied three twin boundary spacings, λ=0.63, 1.25 and 4.38 nm, similar to the samples used in our experiments. An edge crack with atomically sharp tip and length equal to 10% of the sample width was created initially along a twin plane in the mid-portion of the sample. The initial samples were equilibrated using conjugate gradient method and then relaxed at temperature of 1.2 K for 300 ps. Subsequently, uniaxial tension was applied along the vertical direction under strain rate of 1×10^8 s^{-1} and temperature of 1.2 K. The choice of such a low temperature of 1.2 K was to explore the intrinsic brittleness/ductility of the system, as the high strain rate of MD simulations makes it very difficult to decouple the effects of temperature from those of strain rate. During simulations, periodic boundary conditions were imposed in the other two directions.

Figures S6a-d show a sequence of snapshots during the deformation of the λ=4.38 nm sample. It was observed that crack propagated by brittle cleavage along the twin plane until the entire sample failed (see details in Supplementary Movie 1), indicating brittle fracture. However, for the λ=1.25 and 0.63 nm samples, the crack initially propagated along the twin boundary. At the applied strain of 3.56% for λ=0.63 nm and 3.98% for λ=1.25 nm, a pair of twinning dislocations (i.e. Shockley partials) was homogeneously nucleated on the nearest twin boundaries to the crack tip, and then glided on twin planes following the crack. As the applied strain increased, more twinning partials were nucleated on the neighboring twin planes near the crack tip. With further crack propagation, a number of dislocations were nucleated in front of the crack or emitted from the crack tip, leading to crack blunting, and the sample eventually failed due to necking. The above processes are shown in Figures S7a–f and S8a–f, and also in Supplementary Movies S2 and S3. During crack propagation, dislocation

activities resulted in extensive plastic deformation before fracture. This is a manifestation of ductile fracture. In this process, nucleation of twinning dislocations was caused by the stress field of the moving crack tip. Figures S9, S10 and S11 show the distributions of σ_{xx} and σ_{xy} near the crack tip region in the λ=4.38, 1.25 and 0.63 nm samples at different strains, respectively. Contrasting the stress contours among Figures S9–S11 , we find that the twin boundaries near the crack tip in the λ=1.25 and 0.63 nm samples created more confinement for crack propagation than those in the λ=4.38 nm sample. Apparently, in the samples with lower twin boundary spacings, the high shear stresses at the crack tip were sufficient to induce homogeneous nucleation of twinning partial dislocations on neighboring twin boundaries close to the crack tip, which subsequently continuously activated more dislocations upon further crack propagation. These mechanisms give rise to enhanced plasticity (even at low temperature) in the sample at sufficiently small twin boundary spacing. In contrast, the sample with larger twin boundary spacing failed by brittle crack propagation without any dislocation activities.

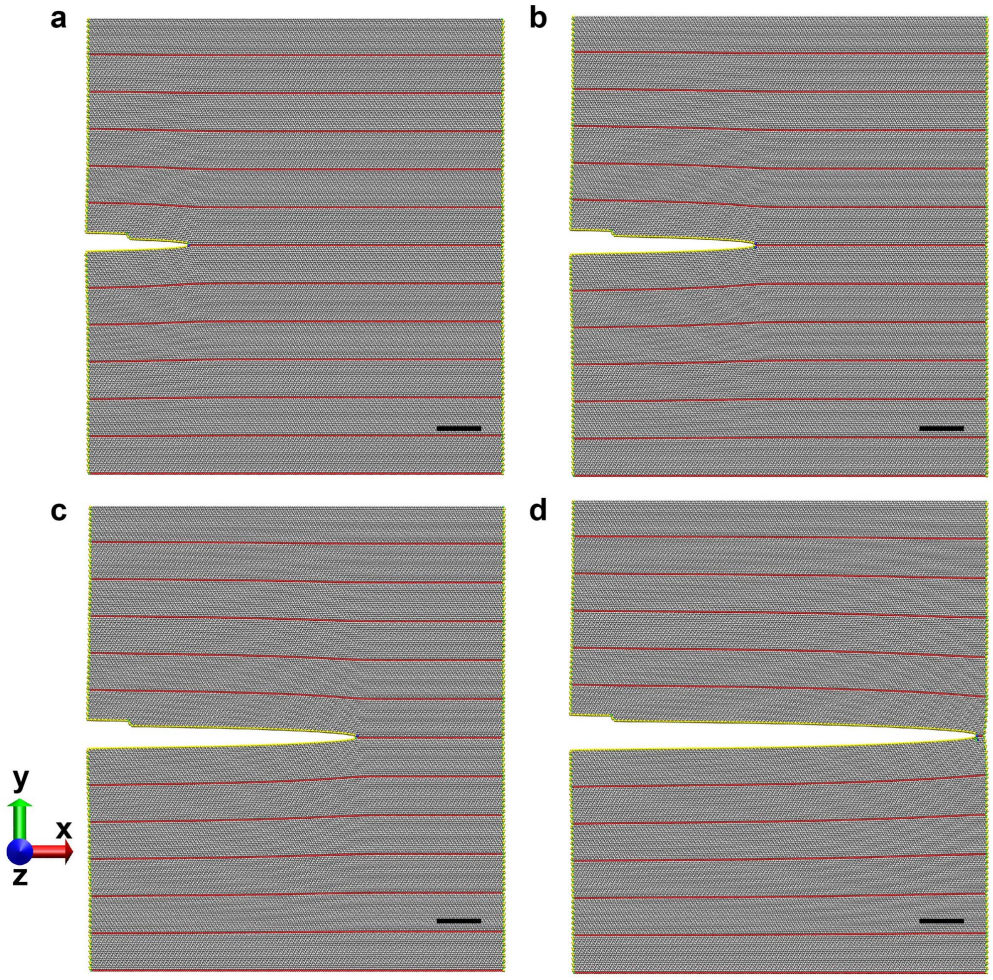

Supplementary Figure S6. **Snapshots of crack propagation in nanotwinned Cu with twin boundary spacing of 4.38 nm at different strains. a,** ϵ=3.56%. **b,** ϵ=4.60%. **c,** ϵ=5.65%. **d,** ϵ=7.47%. Note that the crack propagated by cleavage along the twin boundary. The scale bars are 5 nm.

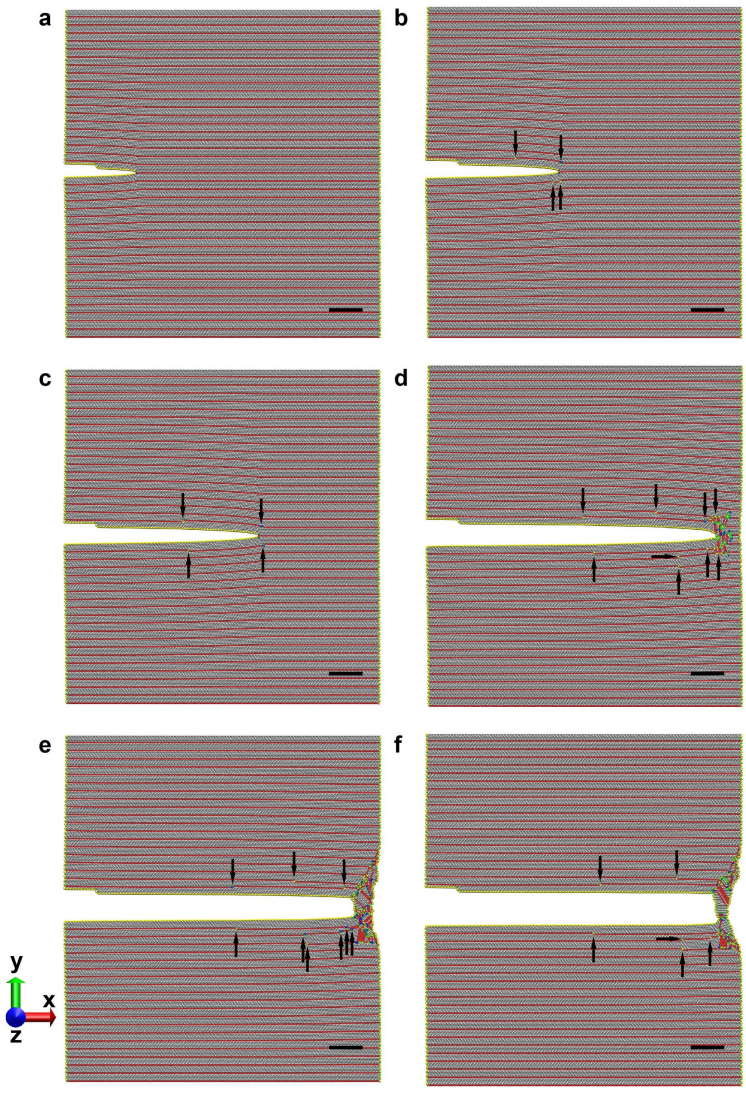

Supplementary Figure S7. **Snapshots of crack propagation in nanotwinned Cu with twin boundary spacing of 1.25 nm at different strains. a,** ϵ=3.56%. **b,** ϵ=4.60%. **c,** ϵ=5.65%. **d,** ϵ=7.79%. **e,** ϵ=9.42%. **f,** ϵ=11.18%. During crack propagation, twinning dislocations are first nucleated on twin boundaries near the crack tip, followed by dislocation emission from the crack tip and crack blunting. Eventually, the sample failed due to necking. Twinning dislocations are indicated by black arrows. The scale bars are 5 nm.

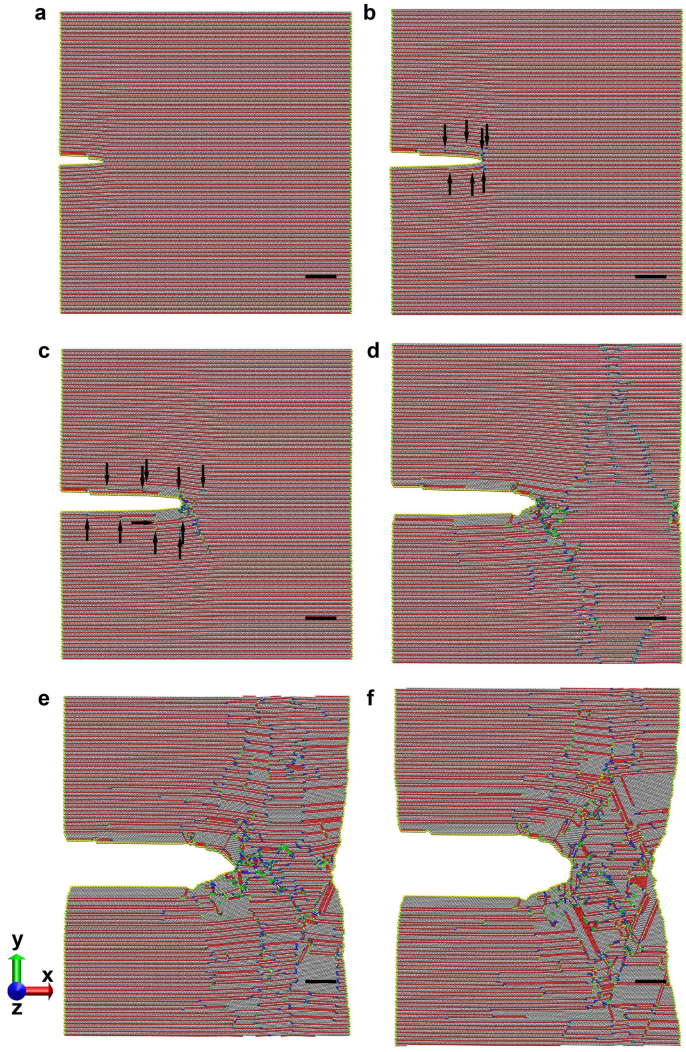

Supplementary Figure S8. **Snapshots of crack propagation in nanotwinned Cu with twin boundary spacing of 0.63 nm at different strains. a,** ϵ=3.25%. **b,** ϵ=4.50%. **c,** ϵ=6.08%. **d,** ϵ=9.31%. **e,** ϵ=16.07%. **f,** ϵ=22.02%. During crack propagation, twinning dislocations are first nucleated on twin boundaries near the crack tip, followed by crack tip emission of dislocations and crack blunting. As applied strain increased, the sample exhibited necking due to massive dislocation activity in front of the crack tip. Some of twinning dislocations are indicated by black arrows. The scale bars are 5 nm.

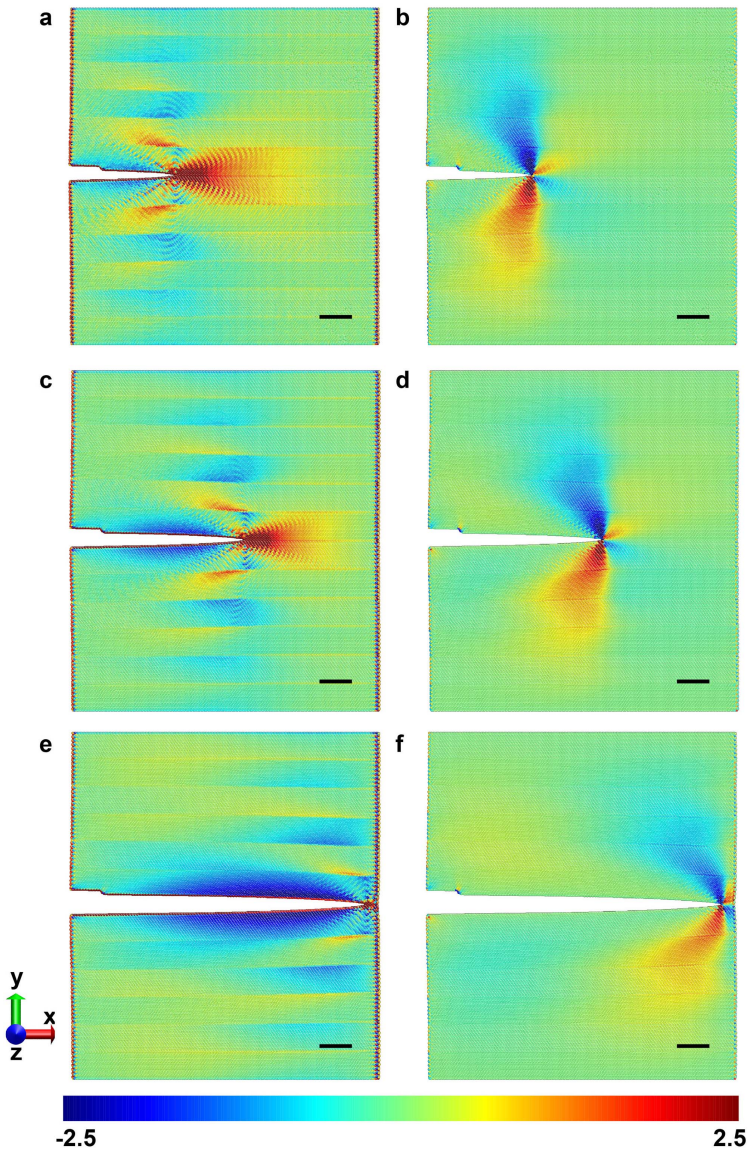

Supplementary Figure S9. **Stress contours near the crack tip region of nanotwinned Cu with twin boundary spacing of 4.38 nm at different strains. a, c** and **e** show the distribution of σ_{xx} at ϵ=4.08%, ϵ=5.23% and ϵ=7.36%, respectively. **b, d** and **d** show the distribution of σ_{xy} at ϵ=4.08%, ϵ=5.23% and ϵ=7.36%, respectively. The scale bars are 5 nm.

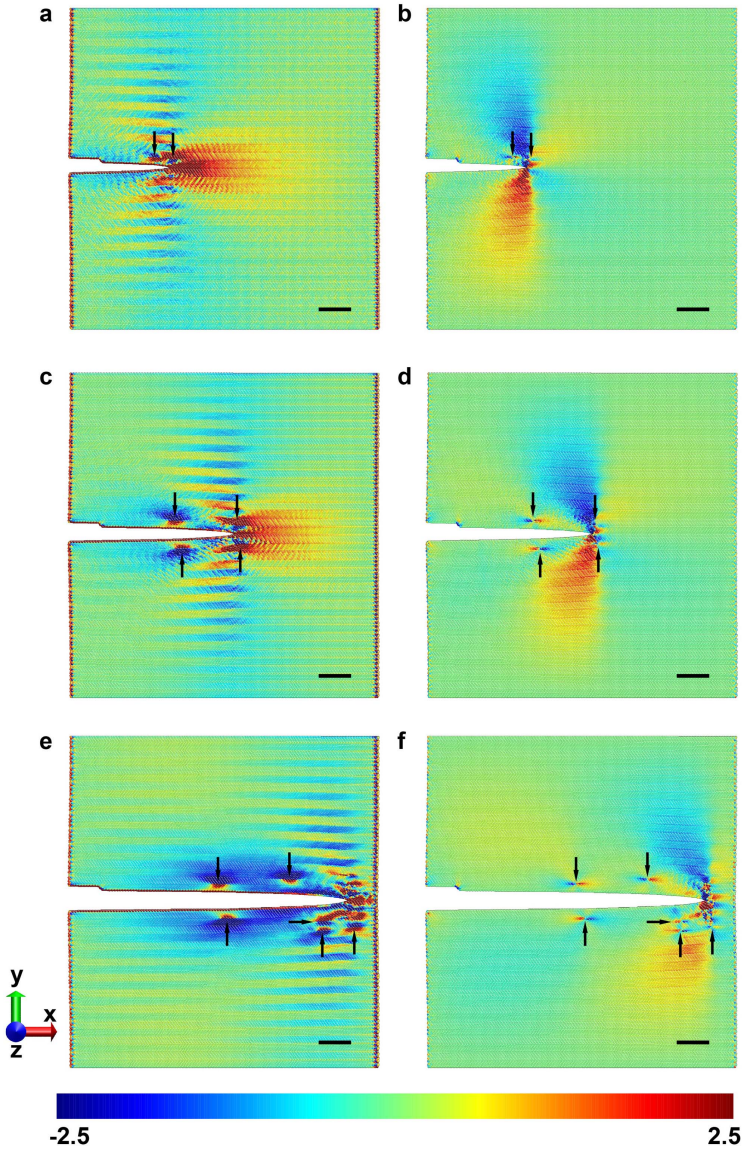

Supplementary Figure S10. **Stress contours near the crack tip region of nanotwinned Cu with twin boundary spacing of 1.25 nm at different strains. a, c** and **e** show the distribution of σ_{xx} at ϵ=4.08%, ϵ=5.23% and ϵ=7.47%, respectively. **b, d** and **d** show the distribution of σ_{xy} at ϵ=4.08%, ϵ=5.23% and ϵ=7.47%, respectively. Some of the twinning dislocations are indicated by black arrows. The scale bars are 5 nm.

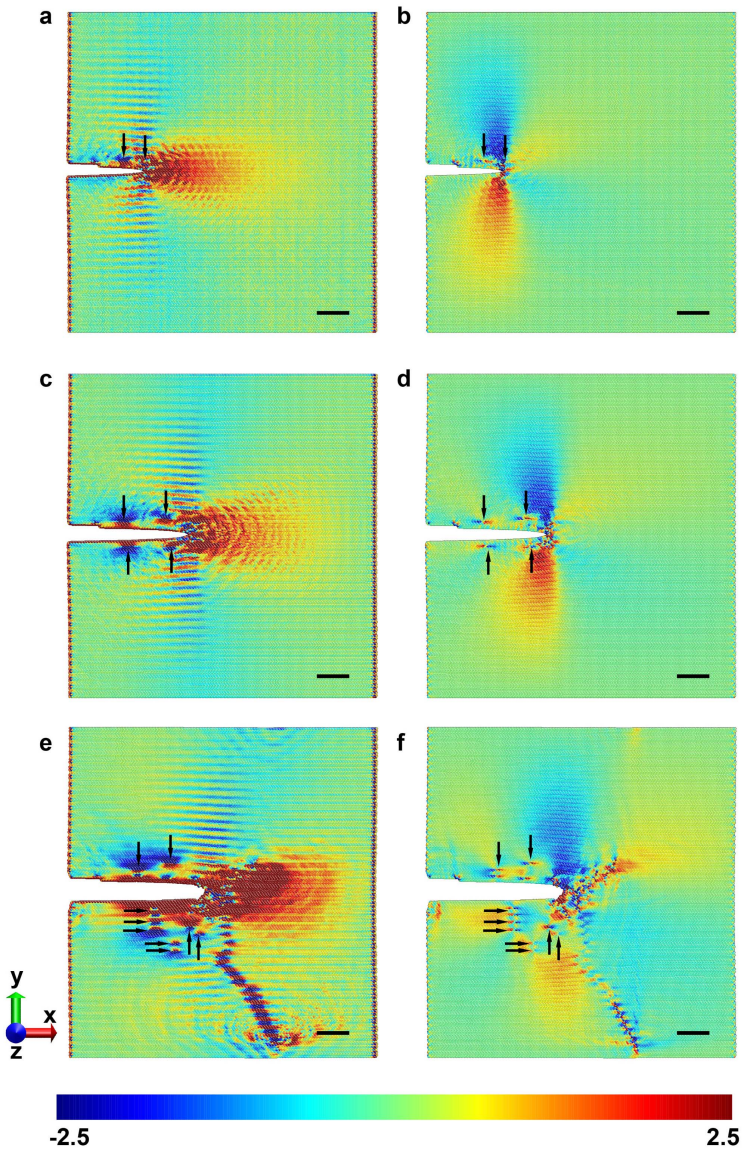

Supplementary Figure S11. **Stress contours near the crack tip region of nanotwinned Cu with twin boundary spacing of 0.63 nm at different strains. a, c** and **e** show the distribution of σ_{xx} at ϵ=3.98%, ϵ=5.13% and ϵ=7.25%, respectively. **b, d** and **d** show the distribution of σ_{xy} at ϵ=3.98%, ϵ=5.13% and ϵ=7.25%, respectively. Some of the twinning dislocations are indicated by black arrows. The scale bars are 5 nm.

B. Theoretical Model

Based on the insights provided by our MD simulations, we have further developed a theoretical model to explain the brittle-to-ductile transition observed in our experiments. The simulations indicate that, at sufficiently small twin spacing, the crack-tip stress field can induce homogeneous nucleation and propagation of twinning partials on twin boundaries in the vicinity of the crack tip, leading to ductile failure in the nanotwinned nanopillars. Figure S12 shows a schematic illustration of twinning dislocation nucleation on a twin boundary adjacent to the crack-tip. Base on Rice's model of dislocation emission from a crack tip[S11] and observations from atomistic simulations, a recent study[S10] has demonstrated that a twin boundary in Cu is intrinsically brittle in the case of crack propagation in the $[1\bar{1}\bar{2}]$ direction along the twin boundary. The energy release rate associated with brittle cleavage along a twin boundary can be expressed as

$$G = 2\gamma_s - \gamma_{tb} \tag{S1}$$

where γ_s is the fracture surface energy and γ_{tb} is the twin boundary energy. The critical stress intensity factor at the crack-tip is

$$K_{Ic} = \sqrt{\frac{2G\mu}{1-\nu}} = \sqrt{\frac{2\mu\left(2\gamma_s - \gamma_{tb}\right)}{1-\nu}} \tag{S2}$$

where μ is the shear modulus and ν the Poisson ratio. The mode-I asymptotic crack-tip field has the following distribution of shear stress,

$$\tau_{xy} = \frac{K_I}{\sqrt{2\pi r}} \cos\frac{\theta}{2} \sin\frac{\theta}{2} \cos\frac{3\theta}{2} \tag{S3}$$

where r and θ are polar coordinates surrounding the crack tip as shown in Figure S12. The resolved shear stress on the twin boundary is thus,

$$\tau_{tb} = \frac{K_I}{2\sqrt{2\pi\lambda}} \sqrt{|\sin\theta|} \sin\theta \cos\frac{3\theta}{2}. \tag{S4}$$

Substitution Eq. S2 into Eq. S4 leads to

$$\tau_{tb} = \frac{1}{2}\sqrt{\frac{\mu\left(2\gamma_s - \gamma_{tb}\right)}{\pi\lambda\left(1-\nu\right)}} \sqrt{|\sin\theta|} \sin\theta \cos\frac{3\theta}{2}. \tag{S5}$$

Note that the effect of crystal anisotropy has been neglected here. It can be shown that the resolved shear stress has its maximum at $\theta \approx 108^\circ$, i.e.,

$$|\tau_{tb}|_{\max} = \alpha\sqrt{\frac{\mu\left(2\gamma_s - \gamma_{tb}\right)}{\pi\lambda\left(1-\nu\right)}} \tag{S6}$$

where $\alpha = 0.441$. Assuming that the homogeneous nucleation of dislocations on a twin boundary would occur when the maximum resolve stress reaches a critical value τ_{crit} , i.e.

$$|\tau_{tb}|_{\max} \geq \tau_{crit}. \tag{S7}$$

Combining Eqs S6 and S7 then leads to the following inequality,

$$\lambda \leq \lambda_{crit} = \frac{\alpha^2 \mu \left(2\gamma_s - \gamma_{tb}\right)}{\pi \tau_{crit}^2 \left(1 - \nu\right)}. \tag{S8}$$

When $\lambda \leq \lambda_{crit}$, twinning dislocations are predicted to nucleate spontaneously on the twin boundary closest to the crack tip before cleavage takes place, even though the twin boundaries themselves are intrinsically brittle, leading to a cascade of dislocation activities and eventually ductile failure. In this process, the twin boundaries near a crack tip become more viable sources of dislocations compared to the crack tip. However, when $\lambda > \lambda_{crit}$, the intrinsically brittle twin boundaries become susceptible to cleavage again in the absence of a viable source near the crack tip. Using the material properties listed in Table S1, the critical twin boundary spacing from Eq. S8 is estimated to be $\lambda_{crit} = 2.37$ nm.

Our experiments showed that the nanotwinned nanopillars with orthogonal twin boundaries exhibited ductile failure when the mean twin boundary spacing was below 2.8 nm, while the sample with twin boundary spacing of 4.3 nm failed in the brittle mode. This implies that the critical twin boundary spacing for brittle-to-ductile transition should be about 3$\sim$4 nm, which is in excellent agreement with the prediction of our model. It is noted that, in evaluating the critical twin spacing from Eq. S8, we have taken the ideal shear strength (2.16 GPa) of Cu from DFT calculations[S12] as the critical shear stress τ_{crit} for homogeneous dislocation nucleation on a twin boundary. In reality, τ_{crit} should be smaller than the ideal shear strength of the material. A 10% reduction of τ_{crit} (to about 1.94 GPa) would cause λ_{crit} to increase by 23% (to 2.93 nm). Figure S13 depicts the homogeneous nucleation of a pair of twinning partials in the sample with twin boundary spacing of 1.25 nm at strain of 3.98%. The point where dislocation nucleation occurs exhibits an angle of 109.5° with respect to the crack-tip, which is also consistent with the corresponding prediction of 108° from our model.

The present model provides a feasible explanation and reasonable critical twin boundary spacing for the observed brittle-to-ductile transition in nanotwinned nanopillars with orthogonal twin boundaries. Note that we have neglected the effects of elastic anisotropy

and free surfaces on twinning dislocation nucleations in the present study. Thus, further investigations are still needed to fully clarify this subject.

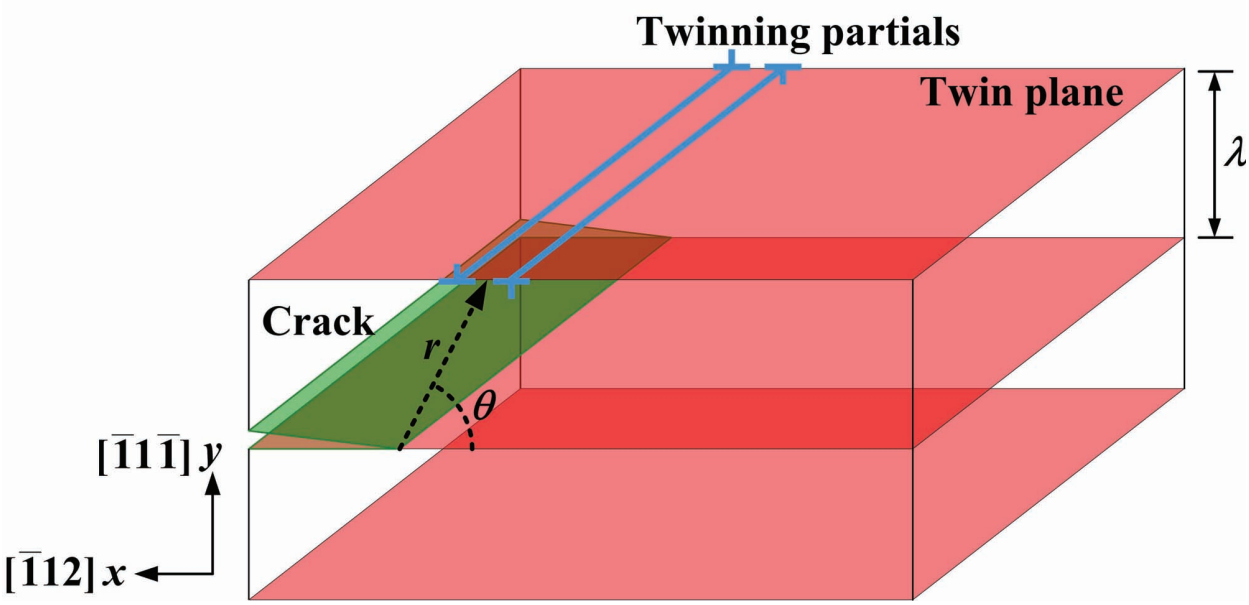

Supplementary Figure S12. **Schematic illustration of homogeneous nucleation of partial dislocations on a twin boundary adjacent to the crack-tip.**

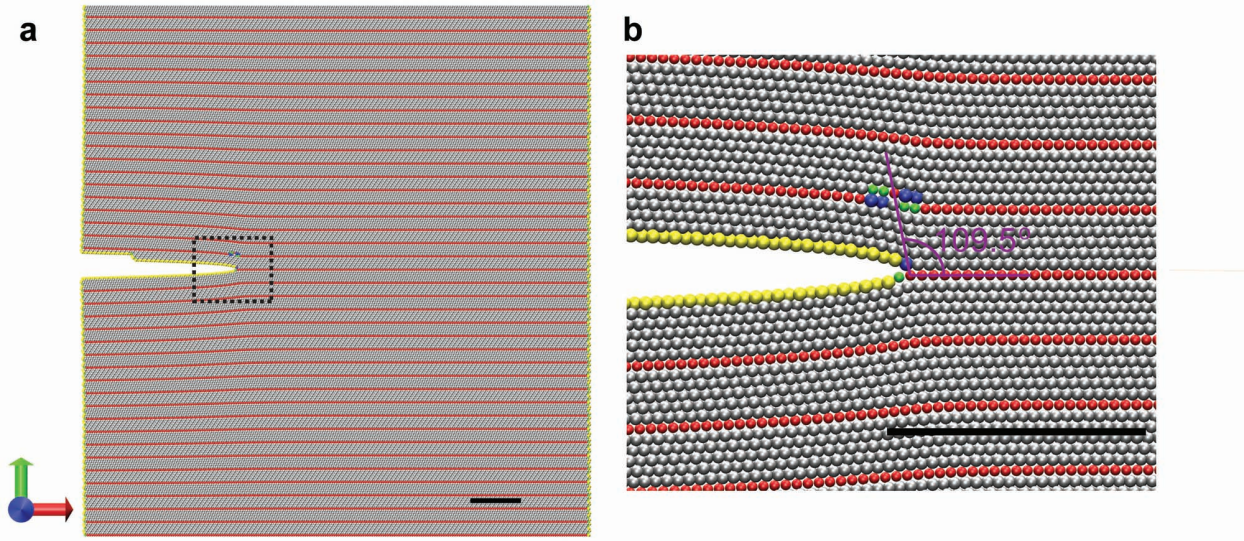

Supplementary Figure S13. **Molecular dynamics simulations of homogeneous nucleation of partial dislocations on a twin boundary adjacent to a crack tip in a nano twinned sample with twin spacing of 1.25 nm under applied strain of 3.98%.** **a,** Full view. **b,** Magnification of region within the dashed rectangle in **a**. All scale bars are 5 nm.

μ(GPa)	μ	γ_s (J/m^2)	γ_{tb} (J/m^2)	τ_{crit} (GPa)
48.0	0.34	1.239	0.022	2.16

TABLE S1. Material properties of Cu

C. Summary

Our atomistic simulations unambiguously demonstrate that twin boundaries can serve as cleavage planes for brittle fracture. We found that when the twin boundaries in nanotwinned Cu are spaced sufficiently close, the high stresses at the crack tip can induce twinning dislocation nucleation and propagation on the twin boundaries in close proximity to the crack tip, leading to a cascade of dislocation activities and eventually ductile failure via plastic deformation. This TB-spacing-induced brittle-to-ductile transition is fully corroborated by our experimental results where the nanopillars with the twin boundary spacings at or below 2.8 nm exhibited clear characteristics of ductile fracture, including extended plasticity and shear localization via necking, at all pillar diameters. In contrast, nanopillars with the larger twin boundary spacing of 4.3 nm failed in a brittle fashion regardless of the pillar size. These distinct deformation mechanisms revealed by atomistic simulations indicate that there exists a twin-spacing-induced transition between intrinsically brittle and intrinsically ductile behaviors in nanotwinned metals, which is consistent with our experimental observations. However, we caution that a more dedicated and systematic study will be needed to fully understand this transition and its implications. This is left to future work.

SUPPLEMENTARY DISCUSSION 3.

A. Discrepancy between molecular dynamics simulations and experiments

When molecular dynamics (MD) simulations are used to study deformation of nanostructured metals, they can provide detailed mechanisms and insights with atomic-level spatial and temporal resolutions to help us understand the microscopic deformation mechanisms. which are not possible to reveal experimentally. In this sense, MD simulations can provide valuable insights that are inaccessible to experiments.

As an atomistic method, MD simulation can only deal with nanoscale objects (typically containing tens of millions of atoms) subject to nearly instantaneous (up to a few nanoseconds) loading and deformation. These inherent limitations in spatial and temporal scales can result in substantial quantitative discrepancies between MD simulations and experiments. So far, MD simulations have been capable of providing mostly qualitative comparisons with experiments. It is expected that the rapid development of supercomputers and advancement in computational technology will continue to improve the length and time scales of MD simulations, so as to reduce the existing gap between simulations and experiments.

In the present work, we combined the experiments with atomistic simulations for their complementary roles in revealing the atomic scale deformation mechanisms in nanotwinned nanopillars. Typically, many internal and external factors are involved in the experiments, while MD simulations are based on idealized models that allow us to focus only on the main factors. In particular, our simulations are focused on the interplay among dislocations, TBs and free surfaces, allowing us to observe strain localization and de-twinning as dominant plastic deformation mechanisms in nanotwinned Cu nanopillars with orthogonal and slanted TBs, respectively. Due to the differences in the deformation mechanisms, the nanotwinned Cu nanopillars with different TB orientations exhibit different yield strengths. These observations are then shown to correlate well with experimental results/observations, and provide the real-time evolution of defects and microstructures (at the atomic scale) under idealized conditions to help us understand the experimental results.

Because of the time-scale limitation, the applied strain rate in MD simulations is about eleven orders of magnitude higher than that used in experiments. When the simulated sample is subjected to a certain macroscopic deformation, high strain rates results in short

relaxation time for atomic motion and interactions, which further induces high stresses. Thus, the simulated system typically exhibits macroscopic stresses higher than those in experiments. Such strain rate effects are frequently observed in atomistic simulations.

In addition, MD simulations are based on idealized systems which ignore many intrinsic complications existing in real experiments. In our simulations, the simulated samples have smooth free surfaces, perfect grain interiors and small aspect ratios. The smooth free surfaces may make dislocation nucleation more difficult compared to that in real materials. Previous study on single crystalline Au nanopillar has indicated that polishing the surface of a nanopillar can produce a striking rise in its yield strength[S13]. We will discuss the influence of surface structures on failure behaviors in the next section. It is obvious that the perfect grain interiors limit the internal dislocation sources or flaws which can significantly reduce the material strength and ductility, so that the simulated sample exhibits high strength and large ductility. Also, in the present simulations, the samples have a small aspect ratio of 3:1. A recent study coupling large scale atomistic simulations and theoretical modeling revealed that the length of Cu nanowires can have significant influence on the failure mode: short nanowires tend to fail in ductile mode through extensive plasticity or necking and have larger ductility, while sufficiently long nanowires exhibit smaller ductility, shear localization and abrupt failure[S14].

B. Failure behaviors of nanotwinned nano pillars/nanowires

To investigate the failure processes of nanotwinned nanopillars/nanowires, we conducted additional simulations of the samples with diameters of 5, 10, 20 nm and twin boundary spacings of 1.25 and 0.63 nm subjected to uniaxial tension. All the simulated samples had the same aspect ratio of 10:1. Furthermore, we also explored the influence of surface structures (or surface defects) on mechanical behaviors of nanopillars/nanowires. We generated two types of samples: one has a smooth (atomically polished) and defect-free surface, and the other has a surface crack with a depth about 8% of sample diameter. To avoid the influence of fixed ends, we imposed periodic boundary conditions along the axial direction of nanopillars. The equilibration and loading processes are the same as those stated in the main manuscript.

Figures S14a and S14b capture a sequence of snapshots of plastic deformation in the 1.25 nm twin spacing sample with defect-free and cracked surfaces, respectively. For the

sample with defect-free smooth surface, localized necking is the primary failure mode, which persists until a single atomic strand prior to fracture, as evident in Figures S14a3∼a6. In contrast, for the sample with surface crack, partial dislocations are found to nucleate and glide near the crack. Such partial slip prevails on a single slip plane in the vicinity of the crack, leading to the formation of a shear band across the sample. Eventually, the sample fails due to shear localization. Similar phenomena are observed during plastic deformation of the nanotwinned sample with twin boundary spacing of 0.63 nm, as shown in Figure S15. Notably, for the sample with defect-free smooth surface, shear localization occurs when partial slip becomes dominant on a single slip plane, as displayed in Figures S15a1∼a2. The sample ruptures with noticeable necking prior to final failure, as shown in Figures S15a5∼a6

Comparing Figures S14a6 and S15a6 with Figures S14b6 and S15b6, we found that the sample with surface crack sustains much smaller fracture stain, relative to the sample with defect-free smooth surface. For example, for the nanotwinned nanopillar with twin boundary spacing of 0.63 nm, the elongation to failure of the cracked sample is only half of that of sample with defect-free smooth surface. Such difference arises from the fact that the shear banding is activated sooner due to the surface crack. It also implies that surface structures (or surface defect) can strongly influence the ductility of nanotwinned nanopillars.

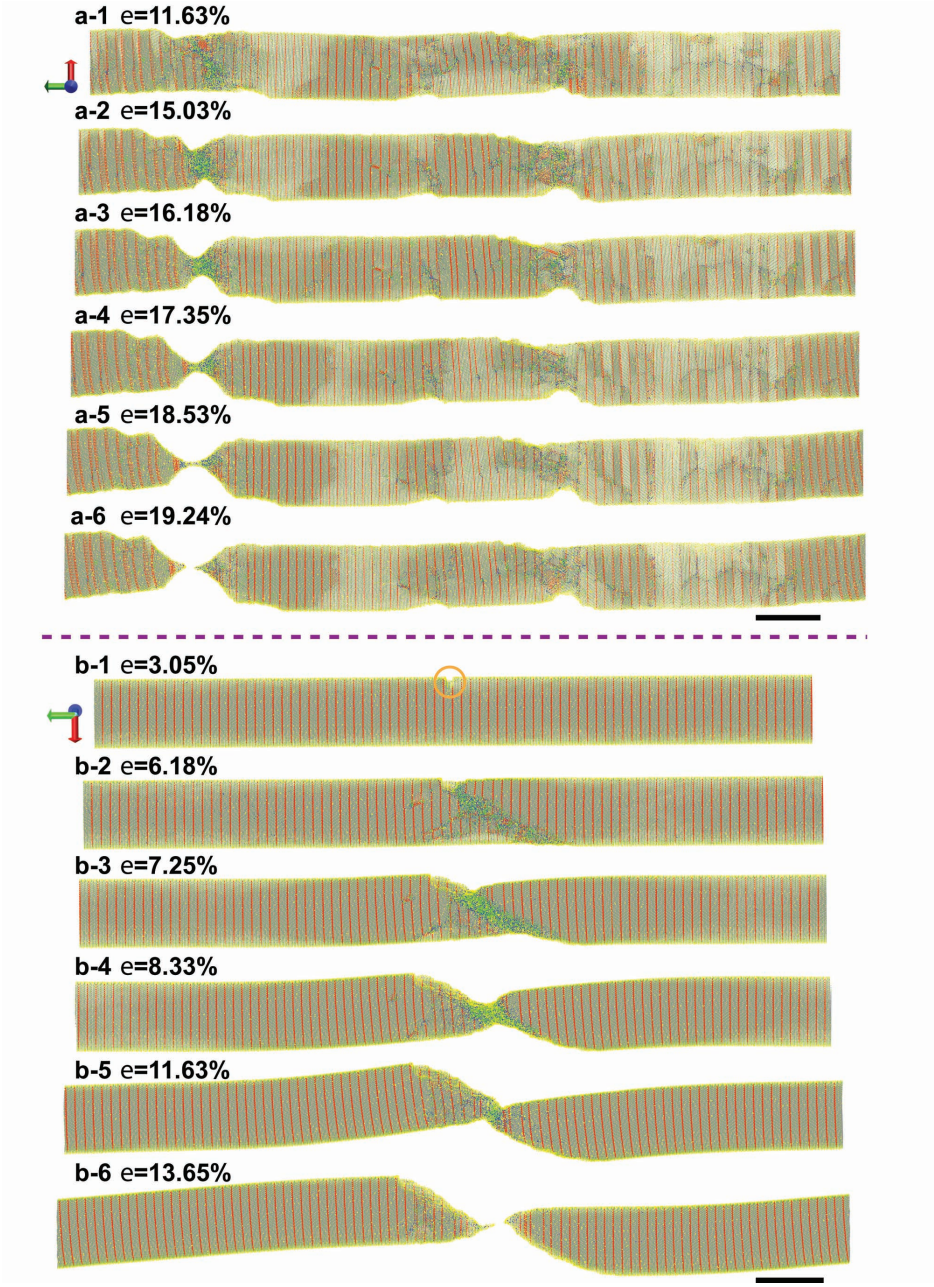

Supplementary Figure S14. **Deformation and failure behaviors of the simulated samples with the orthogonal twin boundaries spaced at an initial interval of 1.25 nm at room temperature.** **a,** Sample with polished defect-free smooth surface. **b,** Sample with a surface crack. All the scale bars are 10 nm.

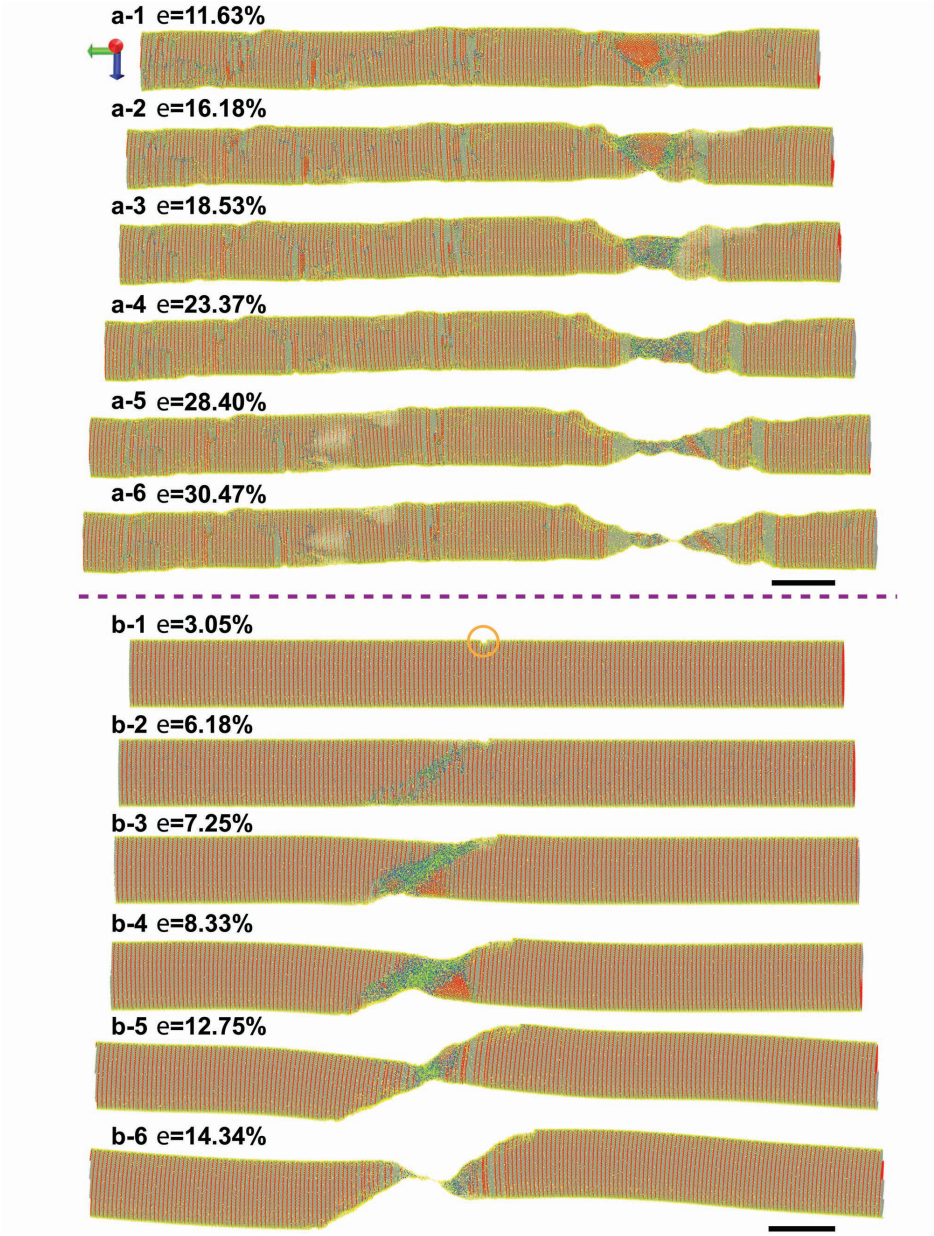

Supplementary Figure S15. **Deformation and failure behaviors of the simulated samples with the orthogonal twin boundaries spaced at an initial interval of 0.63 nm at room temperature. a,** Sample with smooth defect-free surface. **b,** Sample with a surface crack. All the scale bars are 10 nm.

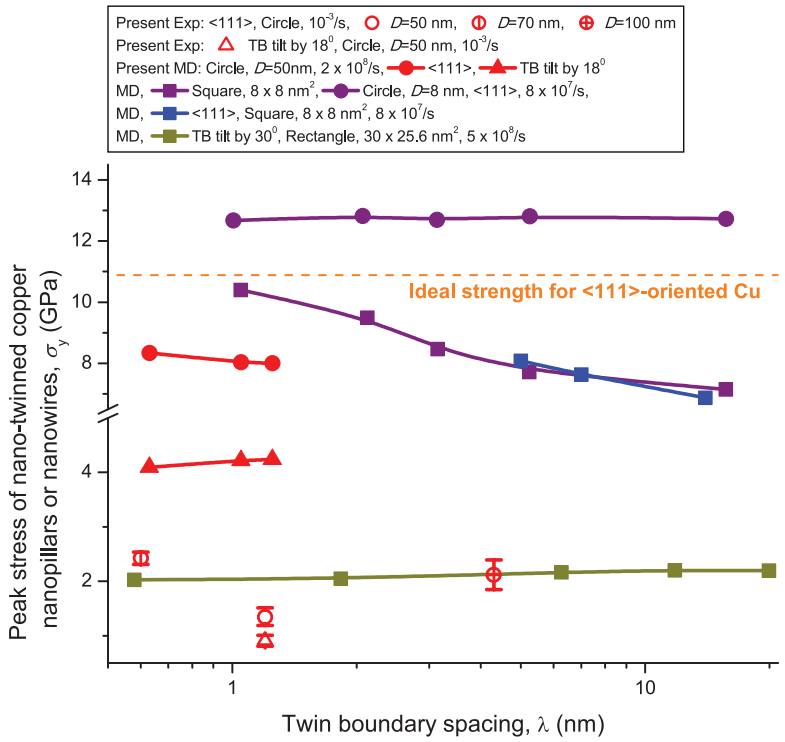

Figure S16. Comparison between present work and other studies. Purple, blue and yellow data are from Refs. [25], [30] and [29] in main text, respectively. Inset key: TB, twin boundary; MD, molecular dynamics; D, diameter; Circle, Square and Rectangle, shape of cross-section.

S1 Beg, M. & Shapiro, S. Study of phonon dispersion relations in cuprous oxide by inelastic neutron scattering. *Physical Review B* **13**, 1728–1734 (1976).

S2 Tan, E. P. S. *et al.* Crystallinity and surface effects on Youngs modulus of CuO nanowires. *Applied Physics Letters* **90**, 163112 (2007).

S3 Zhou, G. Metal-oxide interfaces at the nanoscale. *Applied Physics Letters* **94**, 233115 (2009).

S4 Uchic, M. D., Dimiduk, D. M., Florando, J. N. & Nix, W. D. Oxide surface films on metal crystals - Response. *Science* **306**, 1134–1135 (2004).

S5 Kim, J.-Y. & Greer, J. R. Size-dependent mechanical properties of molybdenum nanopillars. *Applied Physics Letters* **93**, 101916 (2008).

S6 Shan, Z., Mishra, R. K., Syed Asif, S. a., Warren, O. L. & Minor, A. M. Mechanical annealing and source-limited deformation in submicrometre-diameter Ni crystals. *Nature materials* **7**, 115–9 (2008).

S7 Jennings, A. *et al.* Higher compressive strengths and the Bauschinger effect in conformally passivated copper nanopillars. *Acta Materialia* **60**, 3444–3455 (2012).

S8 Richter, G. *et al.* Ultrahigh strength single crystalline nanowhiskers grown by physical vapor deposition. *Nano letters* **9**, 3048–52 (2009).

S9 Lu, Y., Song, J., Huang, J. Y. & Lou, J. Fracture of Sub-20nm Ultrathin Gold Nanowires. *Advanced Functional Materials* **21**, 3982–3989 (2011).

S10 Cheng, Y., Jin, Z.-H., Zhang, Y. & Gao, H. On intrinsic brittleness and ductility of intergranular fracture along symmetrical tilt grain boundaries in copper. *Acta Materialia* **58**, 2293–2299 (2010).

S11 Rice, J. R. Dislocation nucleation from a crack tip: An analysis based on the Peierls concept. *Journal of the Mechanics and Physics of Solids* **40**, 239–271 (1992).

S12 Ogata, S., Li, J. & Yip, S. Ideal pure shear strength of aluminum and copper. *Science* **298**, 807–11 (2002).

S13 Rabkin, E. & Srolovitz, D. J. Onset of plasticity in gold nanopillar compression. *Nano letters* **7**, 101–7 (2007).

S14 Wu, Z., Zhang, Y.-W., Jhon, M. H., Gao, H. & Srolovitz, D. J. Nanowire failure: long = brittle and short = ductile. *Nano letters* **12**, 910–4 (2012).

SUPPLEMENTARY MOVIES CAPTIONS

Supplementary Movie S1. Brittle fracture in nanotwinned Cu with twin boundary spacing of 4.38 nm. A crack cleaves along the twin boundary until the whole sample fails without any dislocation activities.

Supplementary Movie S2. Ductile fracture in nanotwinned Cu with twin boundary spacing of 1.25 nm. During crack propagation along a twin boundary, a pair of twinning partial dislocations (i.e. Shockley partials) are nucleated (at an applied strain of 3.98%) on the nearest twin boundary above the crack tip, and then glide on the twin plane along with the moving crack. As the applied strain further increases, more pairs of twinning partials are nucleated on neighboring twin planes near the crack tip, followed by a cascade of dislocations nucleation events in front of the crack and direct emission from the crack tip, resulting in crack blunting. Finally, the sample fails due to necking from extensive dislocation activities and plastic deformation, indicating ductile fracture.

Supplementary Movie S3. Ductile fracture in nanotwinned Cu nanopillar with twin boundary spacing of 0.63 nm. During crack propagation along a twin plane, twinning dislocations are nucleated on twin boundaries near the crack tip, leading to a cascade of dislocation nucleation events near the crack and direct emission from the crack tip, resulting in crack blunting. The sample eventually fails by necking due to massive dislocation activities in front of the crack tip.

Supplementary Movie S4. Tension experiment on a D250A0 sample. Sample diameter, twin spacing and twin boundary inclination angle are 250 nm, 2.8 nm and 0°, respectively.